metals

MDPI

Article

Effects of Carbon Content on the Properties of Novel Nitrogen-Free Austenitic Stainless Steel with High Hardness Prepared via Metal Injection Molding

Xin Luo [1], Jia Lou [1,2,*], Hao He [3,*], Chu Wu [4], Yuhang Huang [1], Na Su [1] and Shibo Li [1]

[1] School of Materials Science and Engineering, Xiangtan University, Xiangtan 411105, China
[2] Research and Development Department, Taoyuan Institute of Advanced Manufacturing, Foshan 528000, China
[3] School of Microelectronics and Materials Engineering, Guangxi University of Science and Technology, Liuzhou 545006, China
[4] Hunan Hengji Powder Technology Co., Ltd., Yueyang 414517, China
* Correspondence: lou3166@xtu.edu.cn (J.L.); 100001865@gxust.edu.cn (H.H.); Tel.: +86-18670309882 (J.L.); +86-13973114617 (H.H.); Fax: +86-0731-58298498 (J.L.); +86-0722-2687698 (H.H.)

Abstract: A novel nitrogen-free austenitic stainless steel with a hardness of >200 HV was developed using metal injection molding (MIM), and the effects of graphite addition on the sintering behavior, mechanical properties, and corrosion resistance of heat-treated samples were investigated. The results show that a certain amount of graphite addition increases the relative density to >98%. In samples with the addition of 0–500 ppm graphite, large grain-boundary precipitates reduced corrosion resistance and ductility. In contrast, when graphite addition was increased to 750–1500 ppm, fine precipitates, which exhibited coherent lattice relationships with the matrix, were uniformly distributed within the grain and grain boundaries; this significantly improved the mechanical properties and corrosion resistance. The tensile strength and elongation intervals were 546.94–608.62 MPa and 29.68–24.63%, respectively. To prevent overburning, samples with a graphite content higher than 3000 ppm were sintered at a lower temperature, resulting in a higher porosity and lower performance.

Keywords: stainless steel; metal injection molding; graphite addition; mechanical properties; corrosion resistance

Citation: Luo, X.; Lou, J.; He, H.; Wu, C.; Huang, Y.; Su, N.; Li, S. Effects of Carbon Content on the Properties of Novel Nitrogen-Free Austenitic Stainless Steel with High Hardness Prepared via Metal Injection Molding. *Metals* **2023**, *13*, 403. https://doi.org/10.3390/met13020403

Academic Editor: Jose Manuel Torralba

Received: 16 January 2023
Revised: 8 February 2023
Accepted: 10 February 2023
Published: 15 February 2023

1. Introduction

Austenitic stainless steels are widely used in the manufacture of components in the fields of mechanical engineering, medicine, aerospace, and household products because of their excellent ductility, high corrosion resistance, and good surface finish [1–3]. Metal injection molding (MIM) can be used to prepare samples with both high density and good mechanical properties in large quantities and at a low cost [4–6]; austenitic stainless steels, such as 316 L and 304 steels, have been commonly used for this purpose. However, the low hardness of 316 L stainless steel, which is only 140–160 HV, significantly limits its potential to fulfill the increasing demand for high performance and further refinement [6]. Furthermore, it is difficult to achieve the high-volume production of added 316 L stainless steel. Ali et al. [7] and Aslam et al. [8] lowered the sintering temperature and increased the sintering density by adding boron or borides to 316 L stainless steel to improve the mechanical properties of the material; however, the steel fabricated via this method is prone to overburning and boride precipitation, which strongly affect the polishing properties.

Super austenitic stainless steels, such as S32654 [9] and 904 L [10], have been successfully used in ingot casting or machining and can therefore be considered for MIM. However, intermetallic phases frequently precipitate in such steels, which adversely affects the performance of the material [11]. Significantly, nitrogen is always present in these steels, and its solution can refine the grain size of austenitic stainless steel as well as result in a

significant solid-solution strengthening effect. Appropriate nitrogen addition can also aid in controlling the intermetallic phases in super austenitic stainless steels: Zhang et al. [9] reported that a small N content of <900 ppm can decrease and then increase the total amount of precipitation in S31254 austenite, with the corrosion resistance of the steel following the same pattern. However, excessive nitrogen addition leads to the precipitation of nitrides, such as Cr_2N, in steel, which reduces the performance of the material. Therefore, to obtain excellent properties, the nitrogen content of the sample must be precisely controlled. Xu et al. [12] investigated the preparation and sintering behavior of high-nitrogen nickel-free stainless steel for MIM and showed that the nitrogen content varied significantly with temperature during the sintering process and was difficult to precisely control. In addition, under the same conditions, the nitrogen content of samples differed from batch to batch; even in the same batch of samples, the nitrogen content was unstable. Hence, the development of nitrogen-free stainless steel with high hardness is essential to fulfill the requirements for MIM and have significant potential for practical application.

Controlling the carbon content is another key strategy for enhancing the performance of MIM austenitic stainless steels. Similar to the case of nitrogen, the precise control of the carbon content is extremely difficult because injection molding involves adding organic binders, degreasing residues, and sintering for decarburization [13]. For austenitic alloys, such as 304, 316 L, or HK30, the carbon content range is very narrow. Carbon addition not only reduces the sintering temperature and promotes sintering [14], but also imparts austenitic stability and tissue strengthening effects [15]; however, carbon precipitation incurs grain growth and causes oversintering at high concentrations. Significantly, carbides, particularly grain-boundary carbides, reduce corrosion resistance [16,17]. Therefore, in this study, we investigated the effects of the carbon content on the novel MIM stainless steel.

In this study, to overcome the drawback of the insufficient hardness of injection-molded austenitic steels, we designed a new type of nitrogen-free austenitic steel that can satisfy the requirements for injection molding by imitating super austenitic stainless steel. We investigated the microstructure, mechanical properties, and corrosion resistance of heat-treated austenitic stainless steel samples with different concentrations of carbon. The findings of this study will aid the fabrication of strengthened austenitic stainless steel via injection molding in large quantities at an industrial scale.

2. Experimental Section

The experiments were performed using a gas-atomized nitrogen-free austenitic stainless steel powder (D_{50} = 12.21 μm; Hunan Hengji Powder Technology Co., Ltd., Yueyang, China). The chemical compositions of the novel stainless steel powder and the 316 L powder used for comparison are listed in Table 1. The morphologies of the novel stainless steel and graphite powders are shown in Figure 1.

Table 1. Chemical composition of novel nitrogen-free austenitic stainless steel (022Cr21Ni15Mo4Cu3) and 316 L powders produced via gas atomization.

	Element	Cr	Ni	Mo	Cu	Mn	Si	C	O	Fe
Sample A	Content (wt.%)	21.37	15.45	4.41	3.22	0.35	0.47	0.026	0.078	Bal.
316 L	Content (wt.%)	17.80	15.54	2.86	0.33	0.14	0.24	0.022	0.071	Bal

The stainless steel powder was mixed with graphite powder and a multicomponent polyformaldehyde (POM)-based binder using a pressurized twin-screw mixer with a powder loading of 63.8 vol.%. Stainless steel samples with graphite concentrations of 0, 500, 750, 1000, 1500, 2000, 3000, and 5000 ppm were prepared and labeled as samples A, B, C, D, E, F, G, and H, respectively.

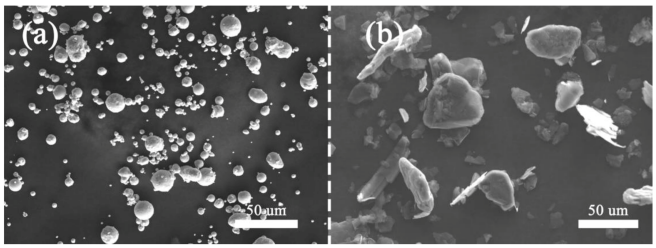

Figure 1. SEM images of (**a**) novel nitrogen-free austenitic stainless steel powder and (**b**) graphite powder.

Green samples of the tensile bars were injection-molded using an injection machine (MIM80, Nuoen, Guangdong, China) at 180 °C and at a pressure of 85 MPa. The green samples were debound in a catalytic degreasing furnace (STE-E, SINTERZONE, Shenzhen, China) to remove most of the POM content, and the remaining binder was thermally degreased. The samples were then sintered in a sintering furnace (VM30/30/100, HIPER, Ningbo, China); the maximum sintering temperature for each sample was determined using JMATPRO calculations and the preliminary experimental results. Sintering was performed at the optimum temperature for 3 h under argon flow (0.15 MPa). The as-sintered samples were vacuum-encapsulated in quartz tubes, solution-treated for 0.5 h at 1200 °C, and subsequently water-quenched. The samples were then aged for 0.5 h at 950 °C before water quenching.

The density was measured using Archimedes' principle, and the carbon and oxygen contents were determined using a carbon/sulfur analyzer (CS2800, NCD, Beijing, China) and oxygen/nitrogen analyzer (ON3000, NCS, Beijing, China), respectively. Three reference groups were tested for samples with different carbon contents. The tensile properties were tested using a universal testing machine (3369, INSTRON, Norwood, MA, USA). The microstructure and fracture morphology of the samples were observed using scanning electron microscopy (SEM; EVO-MA10, Zeiss, Germany), and the elemental distribution of the sintered samples was analyzed using energy dispersive spectroscopy (EDS; OXFORD INCA, Oxford, UK) coupled with SEM. To observe the annealing twins, samples were prepared via electrolytic polishing and analyzed using electron backscattered diffraction (EBSD; EDAX, Mahwah, NJ, USA) with a step size of 2 μm. The physical phases of the different samples were analyzed using X-ray diffractometry (XRD; UItimate IV, RIGAKU, Japan). To determine the type of precipitated phase and the potential phase relationship with the matrix, the samples were prepared via ion thinning and analyzed using transmission electron microscopy (TEM; JEM-2100, JEOL, Japan). Rectangular 10 × 10 mm specimens were cut from the samples and used for corrosion resistance assessment. Electrochemical impedance spectroscopy (EIS) and Tafel curves of the samples were obtained using an electrochemical workstation (REFERENCE 600+, Gamry, Warminster, PA, USA) in a 3.5 wt.% NaCl solution; the samples were immersed in the solution for 1 h before testing.

3. Experimental Results

3.1. Sintering Properties

Table 2 summarizes the chemical compositions, sintering temperatures, relative densities of the sintered samples, and mechanical properties of the heat-treated samples. The relative density of conventional 316 L stainless steel is over 98% at a relatively high sintering temperature of 1400 °C. The novel nitrogen-free austenitic stainless steel with no graphite addition can achieve a similar density at a reduced maximum sintering temperature of 1340 °C, and as the carbon content is increased, the sintering temperature can be further decreased. Figure 2 shows the statistical plots of relative density and carbon and oxygen contents for 316 L stainless steel and the samples with different graphite dosages. The relative density of the 0–2000 ppm graphite-added samples (samples A–F) reaches above 98%, with the sample with 1000 ppm graphite reaching near full density. However, because the samples with high graphite contents were highly susceptible to overburning, a lower

sintering density was applied to samples G and H, resulting in a significantly lower density. When the graphite content was less than 2000 ppm, the carbon reacted with oxygen during the sintering process, causing the oxygen concentration to decrease constantly with increasing levels of graphite addition. However, the oxygen concentration later increased when the porosity increased.

Table 2. Properties of stainless steel samples.

	316 L	A	B	C	D	E	F	G	H
Graphite Dosage (ppm)	0	0	500	750	1000	1500	2000	3000	5000
Sinter Temperature (°C)	1400	1340	1335	1330	1325	1320	1300	1270	1250
Relative Density (%)	98.93	98.70	98.77	98.71	99.87	98.57	98.48	95.53	91.81
Carbon Content (ppm)	103	615	824	1202	1444	1958	2397.2	3120	5176
Oxygen Content (ppm)	370	660	427	330	287	220	170	399	370
Hardness (HV)	150	183.80	184.60	204.73	201.83	213.27	214.23	217.00	214.27
Tensile Strength (MPa)	509.48	508.97	533.78	546.94	558.91	608.62	643.88	432.73	537.74
Yield Strength (MPa)	211.60	213.95	228.59	232.18	242.95	266.27	306.38	236.76	412.77
Elongation (%)	61.17	31.07	31.57	29.68	25.18	24.63	21.38	6.72	3.05

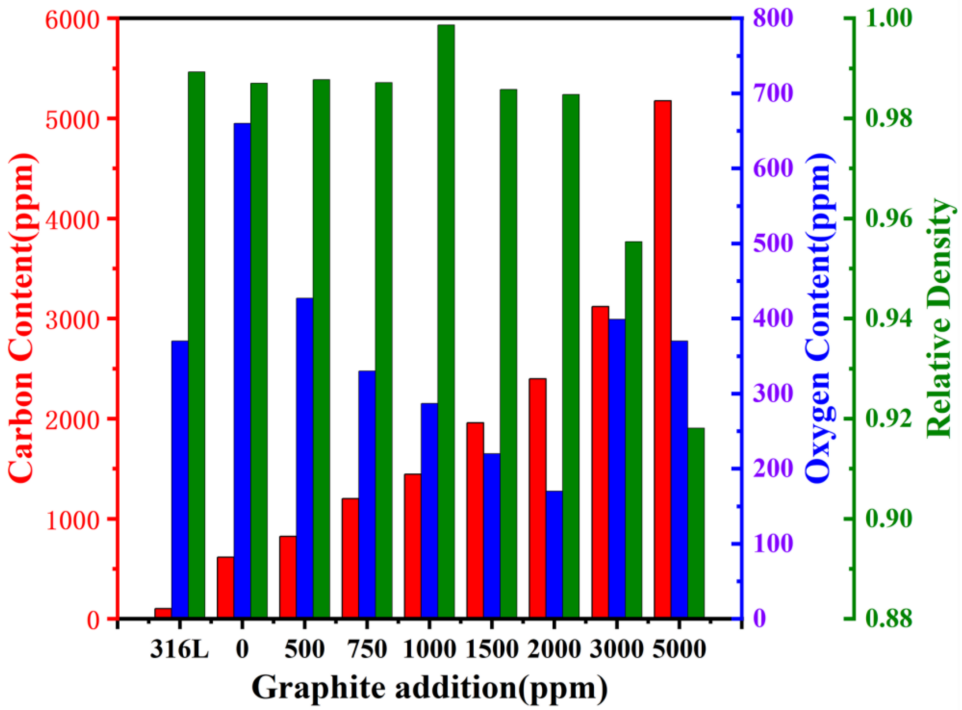

Figure 2. Sintering properties of as-sintered stainless steel samples.

3.2. Microstructure

Figure 3 shows the SEM images of the novel stainless steel samples with different graphite additions; the grain size significantly increases with the carbon content up to 3000 ppm, following which the porosity increases. No intermetallic phases, such as sigma or chi phases, are observed in the samples. Figure 4 shows the precipitate morphology of the different graphite-added samples after heat treatment. Several large precipitates exist along the grain boundaries of samples A and B, and certain grain boundaries consist of continuous short rod-like precipitates, which are identified as carbides. The number of

precipitates increases with increasing carbon addition. In addition, needle-like precipitates and fine precipitate particles are observed near the grain boundaries of sample C. The length of the needle-like precipitates gradually increases with increasing carbon addition content, and consequently, a large number of needle-like precipitates can be observed in sample E. The fine precipitate particles are uniformly distributed within the grain and are increased in number. Large carbide particles can be observed in sample F.

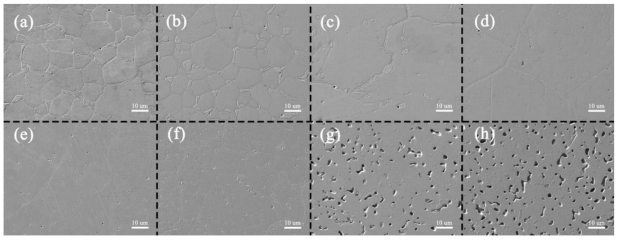

Figure 3. SEM images of heat-treated novel nitrogen-free austenitic stainless steel samples with the addition of (**a**) 0 ppm, (**b**) 500 ppm, (**c**) 750 ppm, (**d**) 1000 ppm, (**e**) 1500 ppm, (**f**) 2000 ppm, (**g**) 3000 ppm, and (**h**) 5000 ppm graphite.

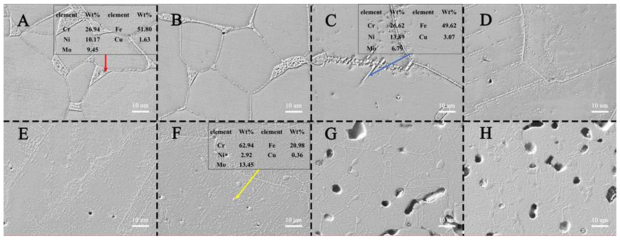

Figure 4. Precipitate morphology of heat-treated novel nitrogen-free austenitic stainless steel samples with the addition of (**A**) 0 ppm, (**B**) 500 ppm, (**C**) 750 ppm, (**D**) 1000 ppm, (**E**) 1500 ppm, (**F**) 2000 ppm, (**G**) 3000 ppm and (**H**) 5000 ppm graphite.

Figure 5 shows the microscopic morphology of the annealed twins in heat-treated samples with different graphite addition levels. Annealing twins are observed in sample B (Figure 5a), and the number of twins increases with increasing carbon content (Figure 5b–f). Figure 5g,h shows the EBSD images of sample B; annealing twins with thicknesses of 2–13 μm are found in almost every grain. Meanwhile, as shown in Figure 5c, the 750 ppm added sample shows a small number of the annealing twins terminating inside several large grains (>150 μm). The intragrain ends of the twins exhibit incoherent twin boundaries, around which a large number of carbides is precipitated. The morphological characteristics are similar to those of 0.3C–20Cr–11Mn–1Mo–0.35N austenitic stainless steel [15].

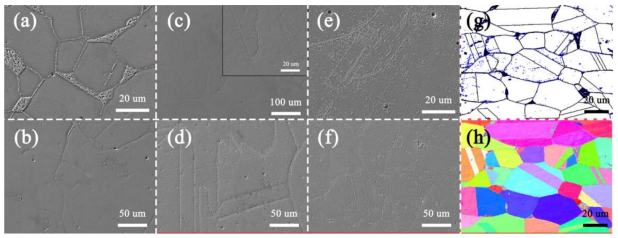

Figure 5. Images of annealed twins in heat-treated novel nitrogen-free austenitic stainless steel samples with the addition of (**a**) 500 ppm, (**b**) 750 ppm, (**c**,**d**) 1000 ppm, (**e**) 1500 ppm, and (**f**) 2000 ppm graphite; (**g**) OIM diagram of sample B; (**h**) IPF diagram of sample B.

The XRD results for the stainless steel show a single austenitic phase. Meanwhile, TEM images confirm the presence of numerous small annealing twin structures, including those in small grains (Figure 6a–c); the boundary spacing between twins is ~25 nm. Figure 6d shows that large amounts of irregularly shaped carbide particles with sizes of 50–150 nm

are present in the matrix. However, with an increase in graphite addition content, the carbides exhibit rhombic or rectangular morphology. Lamellar carbides, as shown in Figure 6e, precipitate along the incoherent twin boundary and are parallel to the coherent twin boundary, representing a phenomenon that is similar to the results of Zheng et al. [15], Lewis et al. [18], Sasmal [19], and others. The effect of these lamellar carbides on the strength is debatable, although several studies have suggested that they are beneficial for corrosion resistance. The selected area electron diffraction (SAED) pattern in Figure 6f shows that the carbides have a co-lattice relationship with the austenite matrix. Figure 6g shows the grain-boundary carbides, and Figure 6h shows the evidence of laminar carbide twins, which also exhibit a co-lattice relationship with the matrix. Larger regular carbide precipitates with sizes of 300–500 nm are observed in sample D, as shown in Figure 6j, and maintain a co-lattice relationship with the matrix. Several large carbides are found in the samples with a carbon content of >2000, as shown in Figure 6k, and their SAED results (Figure 6l) show that they have a non-coherent lattice relationship with the matrix.

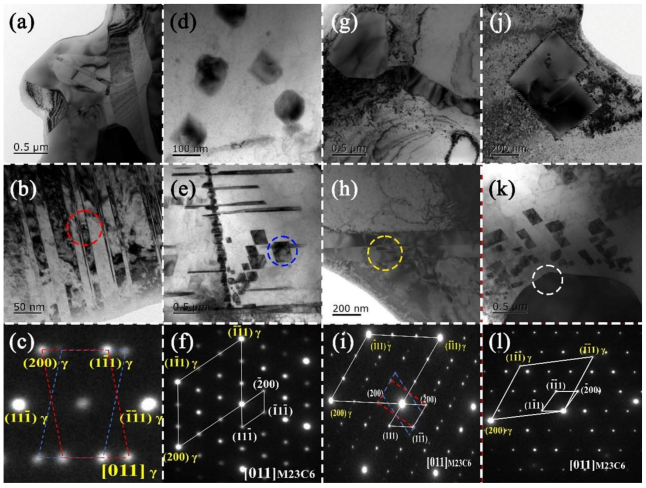

Figure 6. TEM images of stainless steel samples: (**a**) twins in heat-treated sample A; (**b**,**c**) nanotwins and their SAED patterns in sample A, respectively; (**d**) carbide precipitations in sample A; (**e**,**f**) carbides and their SAED patterns in sample C, respectively; (**g**) grain-boundary carbides in sample C; (**h**,**i**) carbide twins and their SAED patterns in sample C, respectively; (**j**) regular carbide in sample D; (**k**,**l**) large carbides and their SAED patterns in sample F, respectively.

3.3. Mechanical Properties

As presented in Table 2, the hardness of the heat-treated samples with different graphite addition levels was higher than 180 HV, which is higher than that of 316 L. The hardness exceeded 200 HV when the graphite addition content exceeded 750 ppm. The hardness remained stable at approximately 210 HV when addition levels exceeded 1500 ppm.

The stress–strain curves of the sintered 316 L and heat-treated stainless steel samples with different graphite addition levels are shown in Figure 7a, and the changes in tensile strength, yield strength, and elongation are shown in Figure 7b. The heat-treated 750–2000 ppm added samples exhibited superior tensile and yield strengths compared to those of 316 L, with the 2000 ppm added samples exhibiting a tensile strength that was 134.4 MPa higher than that of 316 L. However, the ductility of the novel nitrogen-free austenitic stainless steel was lower than that of the 316 L stainless steel and decreased with increasing graphite addition content. Notably, the elongation of all the samples with a graphite content of $\leq$2000 ppm was higher than 20%.

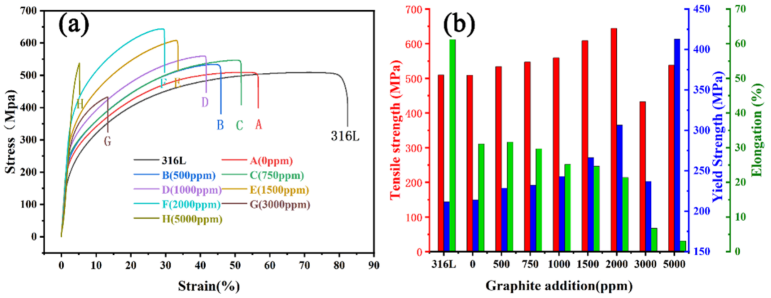

Figure 7. Mechanical properties of sintered 316 L stainless steel and heat-treated novel nitrogen-free austenitic stainless steel samples with the addition of different concentrations of graphite. (**a**) Stress–strain curves; (**b**) tensile strength, yield strength, and elongation.

Figure 8 shows the fracture morphology of the heat-treated samples with different graphite addition levels. The lower graphite-added sample showed a typical inter-crystalline fracture, exhibiting an icing sugar-like fracture. In the 1000 ppm added sample, several fine tough nests are observed, and the fracture surface is rough. With increasing graphite addition content, the icing sugar-like fracture pattern is gradually replaced by fine nests, and the fracture mode changes from inter-crystalline to transgranular fracturing. Notably, the fracture surfaces of the 3000 ppm and 5000 ppm added samples exhibit the original powder boundaries and large pores.

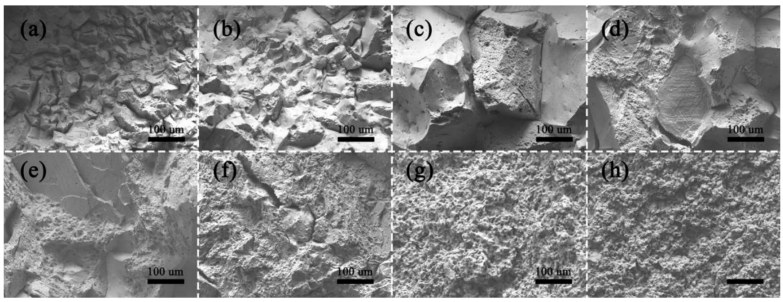

Figure 8. Fracture morphology of heat-treated stainless steel samples with the addition of (**a**) 0 ppm, (**b**) 500 ppm, (**c**) 750 ppm, (**d**) 1000 ppm, (**e**) 1500 ppm, (**f**) 2000 ppm, (**g**) 3000 ppm, and (**h**) 5000 ppm of graphite.

3.4. Corrosion Resistance

The kinetic potential polarization curves of sintered 316 L samples and heat-treated samples with different graphite addition levels are shown in Figure 9, and Table 3 presents the electrochemical corrosion parameters obtained via fitting using the Tafel extrapolation method. The higher the corrosion current density, the lower the corrosion resistance of the material. Samples with a graphite content of ≥2000 ppm exhibited higher corrosion current density than sintered 316 L, whereas samples containing 500–1500 ppm graphite exhibited better corrosion resistance than 316 L.

Table 3. Electrochemical parameters in 3.5% NaCl obtained using a curve-fitting approach.

	316 L	**A**	**B**	**C**	**D**	**E**	**F**	**G**	**H**
Icoor (uA/cm^2)	0.147	0.165	0.015	0.0652	0.0409	0.0541	0.184	0.165	0.161
Ecoor (mV)	−285.33	−290.95	−193.21	−263.68	−268.93	−258.31	−282.96	−283.05	−181.04

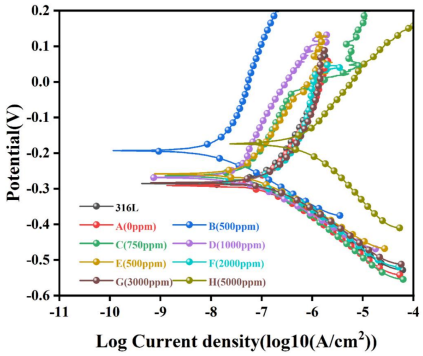

Figure 9. Polarization curves of sintered 316 L stainless steel and novel nitrogen-free austenitic stainless steel samples with the addition of graphite.

The impedance response of the sintered 316 L sample and the novel austenitic stainless steel sample in a 3.5% NaCl solution after 1 h at room temperature (25 °C) is presented in Nyquist and Bode plots, as shown in Figure 10a–c. An equivalent circuit with two time constants (Figure 10d) is proposed to simulate the electrochemical process by analyzing the Nyquist and Bode plots. where Rs is the solution resistance, Rf and Qf are the resistance and capacitance of the passive film, respectively, and Rct and Qdl are the charge transfer resistance and double layer resistance, respectively. The validity of the EIS results was verified by calculating the χ^2 for each sample after curve fitting, which was less than 10^{-3} compared to the experimental data.

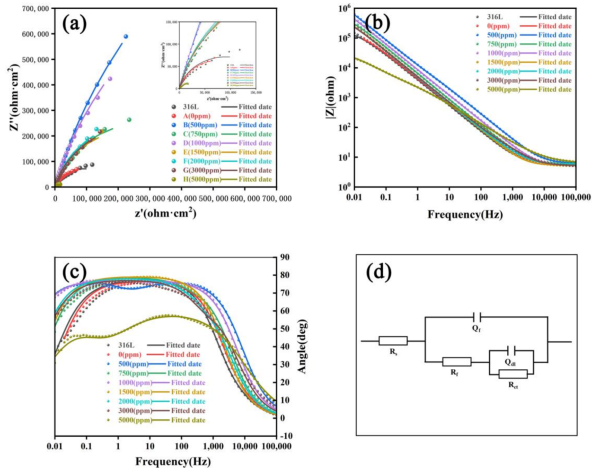

Figure 10. Impedance responses of sintered 316 L stainless steel and heat-treated novel nitrogen-free austenitic stainless steel samples with the addition of different concentrations of graphite. (**a**) Nyquist plot. (**b**,**c**) Bode plots. (**d**) Equivalent electrical circuit used in the ZSimpWin software.

The equivalent circuit fitting data of EIS are presented in Table 4. The charge transfer resistance (Rct) of the heat-treated 0 ppm graphite sample was similar to that of the sintered 316 L sample. In contrast, the Rct of all graphite-added samples, except for the 5000 ppm added sample, was larger than that of the sintered 316 L. The 5000 ppm added sample exhibited an Rct of 37.7 kΩ/cm^2, which was one order of magnitude lower than that of the sintered 316 L sample. The Rct of the 500 ppm and 1500 ppm added samples was one order of magnitude higher than that of the sintered 316 L sample, with the highest Rct reaching 4220 kΩ/cm^2. The Rct is related to the corrosion resistance of the material [20]: the larger the value, the better the corrosion resistance. The Rf values of novel stainless steels were higher than that of 316 L. Considering the polarization and EIS analysis results, samples with graphite concentrations in the range of 500–1500 ppm exhibited superior corrosion resistance compared to that of the sintered 316 L samples.

Table 4. Results of the fitting of equivalent electrical circuit conducted using the ZSimpWin software.

	316 L	A	B	C	D	E	F	G	H
Rs (Ω cm^2)	6.17	5.62	6.05	5.97	5.26	5.21	5.78	5.27	6.25
Qf (10^{-5} Ω^{-1} s^n cm^{-2})	1.42	4.50	1.63	2.72	2.38	3.72	3.18	2.70	10.4
n1	0.951	0.848	0.836	0.874	0.857	0.881	0.872	0.860	0.665
Rf (Ω cm^2)	4.87	17.2	30.1	401	484	123	90.3	68.3	6450
Qdl (10^{-7} Ω^{-1} s^n cm^{-2})	377	27.8	34.2	35.2	1.14	27.1	99.1	136	1420
n2	0.813	0.940	0.863	0.884	0.892	0.933	0.869	0.861	0.711
Rct (kΩ cm^2)	184	163	6740	621	2940	541	681	641	37.7

4. Discussion

4.1. Densification

The sintering of the novel stainless steel can be conducted at a lower temperature than that required for 316 L stainless steel because the former contains a considerable amount of copper, which has a low melting point. Furthermore, carbon addition reduced the Fe–C eutectic point, leading to a high volume of the liquid phase. The sintering window for obtaining highly densified stainless steel is closely related to the volume of the liquid phase [21]. The elimination of closed pores cannot be achieved with very low liquid phase contents, whereas a very high liquid phase content will lead to overburning or poor shape retention. Generally, 5–15 vol.% of liquid phase is recommended in the sintering of commercial stainless steel. Figure 11 shows the temperature–phase composition curves of austenitic stainless steels with different graphite addition levels; the sintering window and applied sintering temperature are also shown. The sintering interval was only 12 °C for sample A but rapidly increased to 32 °C for sample F with 2000 ppm graphite. However, the sintering interval decreased to ~0 °C for the sample with 5000 ppm graphite owing to the early appearance of the liquid phase; therefore, overburning occurred.

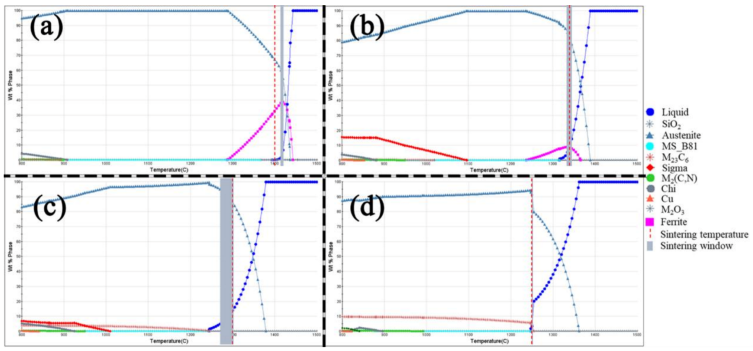

Figure 11. Temperature–phase composition curves of (**a**) 316 L stainless steel and austenitic stainless steels with (**b**) 0 ppm, (**c**) 2000 ppm, and (**d**) 5000 ppm graphite.

4.2. Microstructure Evolution and Strengthening Mechanism

The newly developed nitrogen-free austenitic stainless steel had a higher content of Mo, Cu, and Ni than 316 L stainless steel; hence, a good solid-solution strengthening effect was obtained. While highly alloyed austenitic stainless steel typically undergoes embrittlement owing to the precipitation of sigma- or chi-phase precipitates, achieving a sufficient final carbon content and the use of an appropriate heat treatment suppressed the precipitation of these two phases in the present study [22]. Significantly, graphite addition enhanced the formation of annealing twin structures and precipitation of the $M_{23}C_6$ carbide under the heat-treated condition, which had a significant strengthening effect on the steel [23].

The graphite content has a significant effect on the morphology of carbides in heat-treated samples. For samples with a low addition content (0–500 ppm), carbides tended to nucleate and grow along the grain boundaries, with fewer precipitates within the grain.

This is because grain boundaries have a higher interfacial energy, and therefore, atoms are more likely to expand along the boundaries. Carbides, which preferentially nucleated and grew at the grain boundaries in samples with lower graphite addition contents, did not have a significant strengthening effect on the alloy; instead, they reduced the intergranular bonding. Therefore, the ductility of the alloy was significantly lower than that of 316 L, whereas the strength improvement was negligible. This phenomenon is similar to that reported by Trillo et al. [24], who reported that the threshold value of the carbon content is 500 ppm for 304 stainless steel, and above this value, carbide precipitation at grain boundaries saturates, which increases the possibility of carbide precipitation within the grain, thereby allowing carbide to nucleate at arbitrary locations.

Increasing the graphite addition concentration in heat-treated samples increases the number of carbide nucleation sites and the precipitation probability [24]. At concentrations of 750–1500 ppm, only a small number of bulk precipitates were found at the grain or annealing twin boundaries, most of which were converted into fine granular precipitates distributed along the boundaries, accompanied by long strips of precipitates growing in the grain. Meanwhile, a large number of granular carbides also precipitated in the grain and maintained a co-lattice relationship with the matrix; this precipitation hardening effect significantly strengthened the alloy and reduced the elongation [15]. In samples with an addition content of 750–1500 ppm, these carbide particles gradually grow into rectangular or rhombic shapes (as shown in Figure 10e,j,k) [18] and maintain a co-lattice relationship with the matrix. However, at an addition concentration of 2000 ppm, large granular carbides were formed; these carbides were non-coherent with the matrix and therefore adversely affected the ductility. Because the grain boundaries of the alloy were strengthened by the fine carbides, transgranular fractures appeared on the fracture surface.

Heat-treated samples with a graphite addition concentration of more than 3000 ppm exhibited a significant decrease in strength and elongation owing to a higher porosity, and the presence of coarser carbides may also have contributed significantly. Because of the fine grains and low sintering density, the fracture was dominated by fine tough nests with the original powder boundary rather than fracture along the crystal.

4.3. Corrosion Resistance

The intergranular precipitation of Cr-rich phases leads to the presence of Cr-poor regions near the grain boundaries of austenitic stainless steels, causing intergranular corrosion sensitivity in the samples [16,25,26]. The sample without graphite addition exhibits poorer corrosion resistance after heat treatment than 316 L samples owing to the precipitation of a larger number of massive $M_{23}C_6$ carbides at the grain boundaries, which is consistent with the corrosion current density and Rct values exhibited by the low-carbon content samples. An increase in the graphite addition concentration changed the microstructure of the heat-treated samples, and the number and size of $M_{23}C_6$ carbide precipitates at the grain boundaries of the heat-treated samples decreased at graphite concentrations above 750 ppm, which substantially reduced the intergranular corrosion sensitivity [27]. Owing to its higher Cr, Mo, and Cu contents, the corrosion rate of the surface passivation film was retarded and the film's stability was enhanced [28,29]; hence, the novel stainless steel exhibited a better corrosion resistance than the 316 L sample. Samples with 3000 and 5000 ppm graphite concentrations exhibited a higher porosity, which increased the test area [1,30] under the same chemical test conditions and therefore resulted in inferior resistance compared with that of 316 L.

5. Conclusions

The present work designed a new high-hardness austenitic stainless steel with reference to the composition of super austenitic stainless steels, and samples with different graphite addition were prepared by metal injection molding. The following conclusions were reached:

(1) The novel stainless steel developed in this study achieved a high density at a significantly lower sintering temperature than that of the 316 L stainless steel. However, overburning occurred in samples with graphite concentrations higher than 3000 ppm.
(2) Graphite addition at 500–2000 ppm improved the mechanical properties of the heat-treated novel stainless steel. However, when the graphite addition reached 3000 ppm, the density decreased, and the mechanical properties deteriorated.
(3) Heat-treated samples with different graphite addition levels exhibited different annealing twin and carbide morphologies. In samples containing 0–500 ppm graphite, large carbides precipitated along the grain boundaries, whereas fewer carbides precipitated within the grain. However, when the concentration was between 750 and 1500 ppm, a large number of granular carbides formed, exhibiting a co-lattice relationship with the matrix, which significantly improved the mechanical properties. A graphite concentration higher than 2000 ppm led to the generation of large carbides, which exhibited non-coherent lattice relationships with the matrix.
(4) Large grain-boundary carbides led to the formation of Cr-poor intergranular regions, which reduced the corrosion resistance of the material. Samples with a graphite content in the range of 750–2000 ppm exhibited better corrosion resistance than 316 L stainless steel. Here, the 1000 ppm added samples exhibited the optimal performance.

Author Contributions: X.L.: Validation, Formal analysis, Data Curation, Writing—Original Draft, Visualization, Methodology. J.L.: Conceptualization, Methodology, Resources, Writing—Review and Editing, Project Administration, Funding Acquisition. H.H.: Resources, Funding Acquisition. C.W.: Methodology, Resources. Y.H.: Investigation, Data Curation. N.S.: Investigation, Resources. S.L.: Investigation. All authors have read and agreed to the published version of the manuscript.

Funding: National Natural Science Foundation of China (52164042), Foundation of Hunan Provincial Education Department (21B0121), Open Project of Foshan Taoyuan Advanced Manufacturing (TYKF202203004).

Institutional Review Board Statement: Not applicable.

Informed Consent Statement: Not applicable.

Data Availability Statement: Data will be made available on request.

Acknowledgments: The authors acknowledge support from the National Natural Science Foundation of China (52164042), the Hunan Provincial Education Department Fund (21B0121), and the Foshan Taoyuan Advanced Manufacturing Institute Open Project (TYKF202203004).

Conflicts of Interest: The authors declare that they have no known competing financial interests.

References

1. Pandya, S.; Ramakrishna, K.; Annamalai, A.R.; Upadhyaya, A. Effect of sintering temperature on the mechanical and electrochemical properties of austenitic stainless steel. *Mater. Sci. Eng. A* **2012**, *556*, 271–277. [CrossRef]
2. Yu, K.; Ye, S.; Mo, W.; Lv, Y.; Jiang, H.; Ma, R.; Kwok, C.; Yu, P. Oxygen content control in metal injection molding of 316L austenitic stainless steel using water atomized powder. *J. Manuf. Process.* **2020**, *50*, 498–509. [CrossRef]
3. Zhai, W.; Zhou, W.; Nai, S.M.L. Grain refinement of 316L stainless steel through in-situ alloying with Ti in additive manufacturing. *Mater. Sci. Eng. A* **2022**, *840*, 142912. [CrossRef]
4. Gulsoy, H.O.; Pazarlioglu, S.; Gulsoy, N.; Gundede, B.; Mutlu, O. Effect of Zr, Nb and Ti addition on injection molded 316L stainless steel for bio-applications: Mechanical, electrochemical and biocompatibility properties. *J. Mech. Behav. Biomed. Mater.* **2015**, *51*, 215–224. [CrossRef]
5. Schaper, J.G.; Wolff, M.; Wiese, B.; Ebel, T.; Willumeit-Römer, R. Powder metal injection moulding and heat treatment of AZ81 Mg alloy. *J. Mater. Process. Technol.* **2018**, *267*, 241–246. [CrossRef]
6. Nayak, C.V.; Ramesh, M.R.; Desai, V.; Samanta, S.K. Fabrication of stainless steel based composite by metal injection moulding. *Mater. Today Proc.* **2018**, *5*, 6805–6814. [CrossRef]
7. Ali, S.; Rani, A.M.; Altaf, K.; Baig, Z. Investigation of Boron addition and compaction pressure on the compactibility, densification and microhardness of 316L Stainless Steel. *IOP Conf. Series Mater. Sci. Eng.* **2018**, *344*, 012023. [CrossRef]
8. Aslam, M.; Ahmad, F.; Yusoff, P.; Chai, W.; Ngeow, W.; Nawi, M. Investigation of boron addition on densification and cytotoxicity of powder injection molded 316L stainless steel dental materials. *Arab. J. Sci. Eng.* **2016**, *41*, 4669–4681. [CrossRef]

9. Zhang, S.; Li, H.; Jiang, Z.; Li, Z.; Wu, J.; Zhang, B.; Duan, F.; Feng, H.; Zhu, H. Influence of N on precipitation behavior, associated corrosion and mechanical properties of super austenitic stainless steel S32654. *J. Mater. Sci. Technol.* **2019**, *42*, 143–155. [CrossRef]
10. Sheik, S.; Tirumalla, A.; Gurrala, A.K.; Mohammed, R. Effect of microstructural morphology on corrosion susceptibility of austenitic and super austenitic stainless steels. *Mater. Today Proc.* **2022**, *66*, 514–518. [CrossRef]
11. Zhang, S.; Jiang, Z.; Li, H.; Feng, H.; Zhang, B. Detection of susceptibility to intergranular corrosion of aged super austenitic stainless steel S32654 by a modified electrochemical potentiokinetic reactivation method. *J. Alloys Compd.* **2017**, *695*, 3083–3093. [CrossRef]
12. Xu, Z.-W.; Jia, C.-C.; Kuang, C.-J.; Qu, X.-H. Fabrication and sintering behavior of high-nitrogen nickel-free stainless steels by metal injection molding. *Int. J. Miner. Met. Mater.* **2010**, *17*, 423–428. [CrossRef]
13. Lou, J.; He, H.; Li, Y.; Zhang, H.; Fang, Z.; Wei, X. Effects of Trace Carbon Contents on Lattice Distortion and Nano-Copper Phase Precipitation in Metal Injection-Molded 17-4PH Stainless Steel. *Jom* **2019**, *71*, 1073–1081. [CrossRef]
14. Lou, J.; Liu, M.; He, H.; Wang, X.; Li, Y.; Ouyang, X.; An, C. Investigation of Decarburization Behaviour during the Sintering of Metal Injection Moulded 420 Stainless Steel. *Metals* **2020**, *10*, 211. [CrossRef]
15. Zheng, L.; Hu, X.; Kang, X.; Li, D. Precipitation of M23C6 and its effect on tensile properties of 0.3C–20Cr–11Mn–1Mo–0.35N steel. *Mater. Des.* **2015**, *78*, 42–50. [CrossRef]
16. Zhai, R.; Zhang, H.; Liu, S.; Sun, M.; Sheng, S.; Xu, B. Influence of carbon content on the microstructure and cryogenic tensile properties of N50 austenitic stainless steel after aging treatment. *J. Nucl. Mater.* **2022**, *571*, 154023. [CrossRef]
17. Jones, R.; Randle, V. Sensitisation behaviour of grain boundary engineered austenitic stainless steel. *Mater. Sci. Eng. A* **2010**, *527*, 4275–4280. [CrossRef]
18. Lewis, M.; Hattersley, B. Precipitation of M23C6 in austenitic steels. *Acta Met.* **1965**, *13*, 1159–1168. [CrossRef]
19. Sasmal, B. Mechanism of the formation of lamellar M23C6 at and near twin boundaries in austenitic stainless steels. *Met. Mater. Trans. A* **1999**, *30*, 2791–2801. [CrossRef]
20. Kim, J.; Young, Y. Study on the passive film of Type 316 stainless steel. *Int. J. Electrochem. Sci.* **2013**, *8*, 11847–11859.
21. Bollina, R. Supersolidus Sintering of Boron Added Stainless Steel Powder Compacts. In *European Congress and Exhibition on Powder Metallurgy. European PM Conference Proceedings*; The European Powder Metallurgy Association: Chantilly, France, 2004; Volume 3.
22. Anburaj, J.; Nazirudeen, S.M.; Narayanan, R.; Anandavel, B.; Chandrasekar, A. Ageing of forged superaustenitic stainless steel: Precipitate phases and mechanical properties. *Mater. Sci. Eng. A* **2012**, *535*, 99–107. [CrossRef]
23. Trillo, E.; Murr, L. Effects of carbon content, deformation, and interfacial energetics on carbide precipitation and corrosion sensitization in 304 stainless steel. *Acta Mater.* **1998**, *47*, 235–245. [CrossRef]
24. Trillo, E.; Trillo, E. A TEM investigation of M23C6 carbide precipitation behaviour on varying grain boundary misorientations in 304 stainless steels. *J. Mater. Sci.* **1998**, *33*, 1263–1271. [CrossRef]
25. Chen, G.; Rahimi, R.; Harwarth, M.; Motylenko, M.; Xu, G.; Biermann, H.; Mola, J. Non-cube-on-cube orientation relationship between M23C6 and austenite in an austenitic stainless steel. *Scr. Mater.* **2022**, *213*, 114597. [CrossRef]
26. Kolli, S.; Javaheri, W.; Kömi, J.; Porter, D. On the role of grain size and carbon content on the sensitization and desensitization behavior of 301 austenitic stainless steel. *Metals* **2019**, *9*, 1193. [CrossRef]
27. Li, S.-X.; He, Y.-N.; Yu, S.-R.; Zhang, P.-Y. Evaluation of the effect of grain size on chromium carbide precipitation and intergranular corrosion of 316L stainless steel. *Corros. Sci.* **2013**, *66*, 211–216. [CrossRef]
28. Zhang, S.; Li, H.; Jiang, Z.; Zhang, B.; Li, Z.; Wu, J.; Fan, S.; Feng, H.; Zhu, H. Effects of Cr and Mo on precipitation behavior and associated intergranular corrosion susceptibility of superaustenitic stainless steel S32654. *Mater. Charact.* **2019**, *152*, 141–150. [CrossRef]
29. Li, B.; Qu, H.; Lang, Y.; Feng, H.; Chen, Q.; Chen, H. Copper alloying content effect on pitting resistance of modified 00Cr20Ni18Mo6CuN super austenitic stainless steels. *Corros. Sci.* **2020**, *173*, 108791. [CrossRef]
30. Bayraktaroglu, E.; Gulsoy, H.O.; Gulsoy, N.; Er, O.; Kilic, H. Effect of boron addition on injection molded 316L stainless steel: Mechanical, corrosion properties and in vitro bioactivity. *Bio-Med. Mater. Eng.* **2012**, *22*, 333–349. [CrossRef]